



Numerical Simulation of Hurricane Bonnie (1998). Part III: Energetics

WALLACE HOGSETT AND DA-LIN ZHANG

Department of Atmospheric and Oceanic Science, University of Maryland, College Park, College Park, Maryland

(Manuscript received 29 January 2009, in final form 13 March 2009)

ABSTRACT

Despite considerable research on tropical cyclones (TCs), few studies have been performed to examine inner-core energy conversions because of the lack of high-resolution data. In this study, the TC energetic characteristics in relation to intensity and structural changes under different sheared environments are investigated using a 5-day cloud-resolving simulation of Hurricane Bonnie (1998). Results show that in the presence of intense vertical shear Bonnie undergoes high-frequency fluctuations in intensity and energy conversions (at a time scale of 3 h) during the partial eyewall stage. The fluctuations are closely related to the life cycle of individual convective elements that propagate cyclonically around the downshear portion of the eyewall. The energy conversions are shown to be maximized in the vicinity of the radius of maximum wind (RMW), thus affecting strongly TC intensity. On average, about 2% of latent energy can be converted to kinetic energy to increase TC intensity. After the vertical shear subsides below a threshold, intensity fluctuations become small as convective elements reorganize into an axisymmetric eyewall in which energy conversions are more evenly distributed.

Fourier decomposition is conducted to separate the wavenumber-0, -1, and -2 components of inner-core energetics. Whereas wavenumber-1 perturbations dominate the partial eyewall stage, the propagation of wavenumber-2 perturbations is shown to be closely related to individual convective elements during both the partial eyewall and axisymmetric stages. The wavenumber-2 perturbations can be traced as they move around the eyewall in the form of vortex-Rossby waves, and they play a role in determining the large intensity fluctuations during the partial eyewall stage and the formation of an outer eyewall to replace the partial inner eyewall at the later stage.

1. Introduction

Tropical cyclones (TCs) devastate life and property by concentrating large amounts of kinetic energy (KE) within a small radius in the inner-core regions. Most of the KE is generated through a continuous series of energy conversions, with the latent energy (LE) as the fundamental source, which is obtained primarily through upward fluxes of latent heat from the underlying warm ocean and released in convective clouds in the eyewall. Some of the released LE is used to increase KE via pressure adjustment to the gradient-wind balance, and the location and quantity of such energy transformations dictate the intensification rate of TCs.

Several observational and modeling studies have been performed to understand the KE production in relation

to LE in TCs. Frank (1977) used composites of rawinsondes to calculate the KE and moist static energy budgets of TCs and showed how TCs import KE from their environment and produce most KE in the near-surface layer. McBride (1981) composited data from both the Atlantic and Pacific basins to calculate energy budgets for different tropical cloud clusters. It was found that intensifying storms are characterized by a synoptic-scale increase in KE and a decrease in LE, which is consumed through latent heat release (LHR). Both studies, however, were limited by the poor resolution of observations from investigating the energetic processes of an individual storm. The lack of observations over the tropical oceans is particularly troublesome for studying important energetic processes that occur in the inner-core convective regions, which are not conducive to in situ measurements.

However, the ability of mesoscale models to reproduce the structures and evolution of TCs and provide dense, high-quality data is continually increasing. For example, Tuleya and Kurihara (1975) used the Geophysical Fluid

Corresponding author address: Dr. Da-Lin Zhang, Dept. of Atmospheric and Oceanic Science, University of Maryland, College Park, College Park, MD 20742-2425.
E-mail: dalin@atmos.umd.edu

Dynamics Laboratory (GFDL) TC model to simulate an idealized TC, and they calculated budgets of mean and eddy KE, as well as LE, at different stages of storm development. They found that the KE budgets are determined primarily by the mean flow, although the contribution of eddies is not negligible. Wang (2002a) also examined the inner-core energetics of a simulated TC vortex and found that the maximum eddy KE, located in the lower levels near the radius of maximum wind (RMW), appears to be associated with vortex–Rossby waves (VRWs). Although VRWs have been hypothesized to be active in the inner core of TCs (Montgomery and Kallenbach 1997) and have been observed using radar data (Reasor et al. 2000; Corbosiero et al. 2006) and simulated in high-resolution models (e.g., Wang 2001, 2002a,b), nonetheless their roles in intensity changes remain unclear. Corbosiero et al. (2006) showed that wavenumber-2 features propagate around the eyewall of a vertically sheared hurricane and resemble theoretical VRWs in their tangential and outward propagation speeds. VRWs may develop as a result of barotropic instability in the eyewall (Kossin et al. 2000) or vertical shear (Reasor and Montgomery 2001). But the relative active or passive nature of the waves in TC intensity changes remains elusive.

Recently, cloud-resolving models have been successfully applied to simulating the structures and evolution of hurricanes with real observations at very high resolution (e.g., Liu et al. 1997; Braun 2002; Zhu et al. 2004, hereafter Part I) and they have evolved to the point where they can be used to confidently investigate the inner-core dynamics of individual storms. Given the observational limitations, such real-data simulations could provide dynamically consistent data to study energetic and wave characteristics of TCs. Thus, the purposes of this study are (i) to present the three-dimensional (3D) structures and evolution of hurricane energetics in relation to intensity and structural changes during its life cycle, (ii) to provide insight into the energy conversion processes that link the TC energetics, and (iii) to examine the roles of deep convection and VRWs in determining the hurricane intensity and structural fluctuations. These will be achieved by performing quasi-Lagrangian budget analyses of a cloud-resolving simulation of Hurricane Bonnie (1998) using the fifth-generation Pennsylvania State University–National Center for Atmospheric Research Mesoscale Model (MM5), as described in Part I. In Zhu and Zhang (2006a, hereafter Part II) numerical experiments were conducted to test the sensitivity of the simulation to microphysical processes, which expectedly play a significant role in the intensification of the storm.

The next section provides a brief review of Hurricane Bonnie (1998) and the model simulation from Part I.

Section 3 presents the budget equations used for the study. Section 4 shows time series of the storm-integrated KE and LE budgets. Section 5 examines the 3D structures of the energy conversion processes. Section 6 shows the evolution of the mean and eddy components of KE and relates the KE intensity changes to the azimuthal and radial propagations of VRWs during two different stages of Bonnie. A summary and concluding remarks are given in the final section.

2. Overview

During its lifetime, Bonnie underwent a complex intensity and structural evolution. Airborne radar observations show that the eyewall was highly asymmetric during 22–25 August 1998—a period of rapid intensification—and then it evolved through an eyewall replacement into a more axisymmetric structure during 25–27 August, prior to landfall. The structural evolution can be explained in terms of vertical wind shear that was strongest during the partial eyewall stage and then weakened to allow for axisymmetrization. That is, the highest radar reflectivity occurred on the downshear (left) side of the shear vector with a wavenumber-1 asymmetry early in Bonnie's lifetime, and Bonnie began to transition to a more classic axisymmetric TC devoid of significant asymmetric structures as the shear subsided on 24 August.

Observational studies of Bonnie suggest that her structural evolution is more complicated than the above description. Heymsfield et al. (2001) used satellite and airborne radar data to show that during the partial eyewall stage several convective cells developed and decayed, one after the other, on the downshear side of the vortex. They showed that convective cells developed downshear and progressed cyclonically around the downshear (left) half of the storm. They suggested that downdrafts inside the eye, associated with the episodic vigorous eyewall updrafts, may enhance the warm core of the storm. Molinari and Vollaro (2008) used dropsondes and satellite data to show that the downshear side of Bonnie not only exhibited episodic cellular convection but also contained a sufficient balance of instability and vertical shear to support supercells, similar to those observed in the mid-latitudes. Supercells are well known to have longer lifetimes than convective cells that occur in the absence of vertical shear.

Part I shows that the MM5 simulation of Bonnie agrees quite well with the observed track, structure, and intensity. As observed, the simulated Bonnie exhibits rapid intensification ending at 48 h into the simulation and subsequently maintains her intensity, except for some slight oscillations due to an eyewall replacement cycle. The simulated Bonnie also exhibits the shear-forced

wavenumber-1 reflectivity pattern that evolves into axisymmetry as the vertical shear subsides.

In this study, we utilize the same model simulation at the finest mesh size of 4 km that was used in Part I, but with the model output at time intervals of 15 min, which will allow for the emergence of details that are not apparent in the 6-hourly output data used in Part I. A time series of storm intensity, given in Fig. 1, shows that the general evolution resembles that shown in Part I: rapid intensification (36–48 h), maintenance (48–66 h), and finally a weakening (66–81 h) and reintensification (81–96 h). The latter two phases are associated with an eyewall replacement cycle, which is characterized by the decay of the shear-forced partial eyewall centered around $R = 50$ km (Fig. 2a) and the subsequent reintensification through the replacement of the inner eyewall by an outer axisymmetric eyewall centered around $R = 100$ km (Fig. 2b). This eyewall replacement occurs as Bonnie moves into an environment with decreasing vertical shear (Part I).

It should be mentioned that the time series of the maximum surface wind, shown in Fig. 1, exhibits more significant fluctuations than that in Part I because of the use of 15-min model output here. The fluctuations during 36–66 h, reaching 10 m s^{-1} , are semiregular with a period of 2–5 h, and they are not “numerical noise” but instead are related to hurricane intensity changes. In fact, the period with high-amplitude fluctuations coincides with the period when vertical shear is larger than 12 m s^{-1} (see Fig. 8). Thus, as one of the objectives of this study, we wish to understand the origin and mechanisms of the high-frequency intensity fluctuations from an energetics point of view.

Because Part I has shown many 3D structures of Bonnie, we will focus here on the energetics during the following two characteristic stages of Bonnie: the asymmetric and axisymmetric stages. During the asymmetric partial eyewall stage, the vertical shear vector points from west-northwest to east-southeast (Fig. 2a), so the maximum low-level KE and radar reflectivity are collocated in the downshear (left) half of the eyewall, with some slight phase difference. The KE and radar reflectivity also exhibit asymmetric structures along the west–east cross section, with a greater vertical extent on the eastern side due to downshear-enhanced vertical motion (Fig. 2c). A secondary effect of the vertical shear is the downshear tilt of the vortex.

As the vertical shear decreases to less than 5 m s^{-1} , both the KE and radar reflectivity evolve to axisymmetry in the horizontal (Fig. 2b) and vertical (Fig. 2d). That is, the shear-forced horizontal wavenumber-1 structures have nearly disappeared, and the eyewall evolution can be described in the context of persistent wavenumber-2

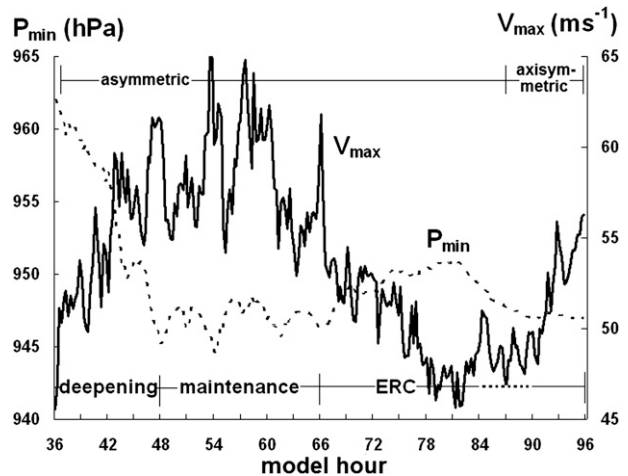


FIG. 1. Time series (15 min) of the minimum central pressure (dashed; hPa) and the maximum surface winds (solid; m s^{-1}) from the 36–96-h simulation. The three characteristic stages of deepening, maintenance, and eyewall replacement (ERC) are delineated (bottom line), as well as the asymmetric and axisymmetric stages (top line). The dotted segment of the ERC stage (84–90 h) denotes the period in which the most rapid transition to axisymmetry occurs.

features, as will be shown in section 6. Of interest is that during this later stage larger KE is distributed over a larger area in the eyewall (cf. Figs. 2a,b), whereas the maximum surface wind is actually smaller (Fig. 1). In the vertical, Bonnie shows a classic axisymmetric upright vortex, with low-level inflow, outward-sloping eyewall updrafts, and upper-level outflow (Fig. 2d). The remainder of this study will focus on the energetic mechanisms by which Bonnie undergoes rapid intensity fluctuations during the partial eyewall stage and on how she transitions between these extreme states of asymmetry and axisymmetry via an eyewall replacement.

3. Energy equations

In this study, quasi-Lagrangian budget equations for LE, KE, and total potential energy (TPE) are derived based on the nonhydrostatic MM5 system (Dudhia 1993). Table 1 summarizes the energetic quantities used in this study. Various energies per unit volume (J m^{-3}) are defined as

$$\text{LE} = \rho L_v q_v,$$

$$\text{TPE} = \rho(c_v T + gz) = \text{IE} + \text{PE}, \quad \text{and}$$

$$\text{KE} = \rho \frac{\mathbf{V}_h \cdot \mathbf{V}_h}{2},$$

where \mathbf{V}_h is the horizontal velocity with respect to the ground, q_v is the water vapor mixing ratio, L_v is the latent heat of vaporization, c_v is the specific heat at constant

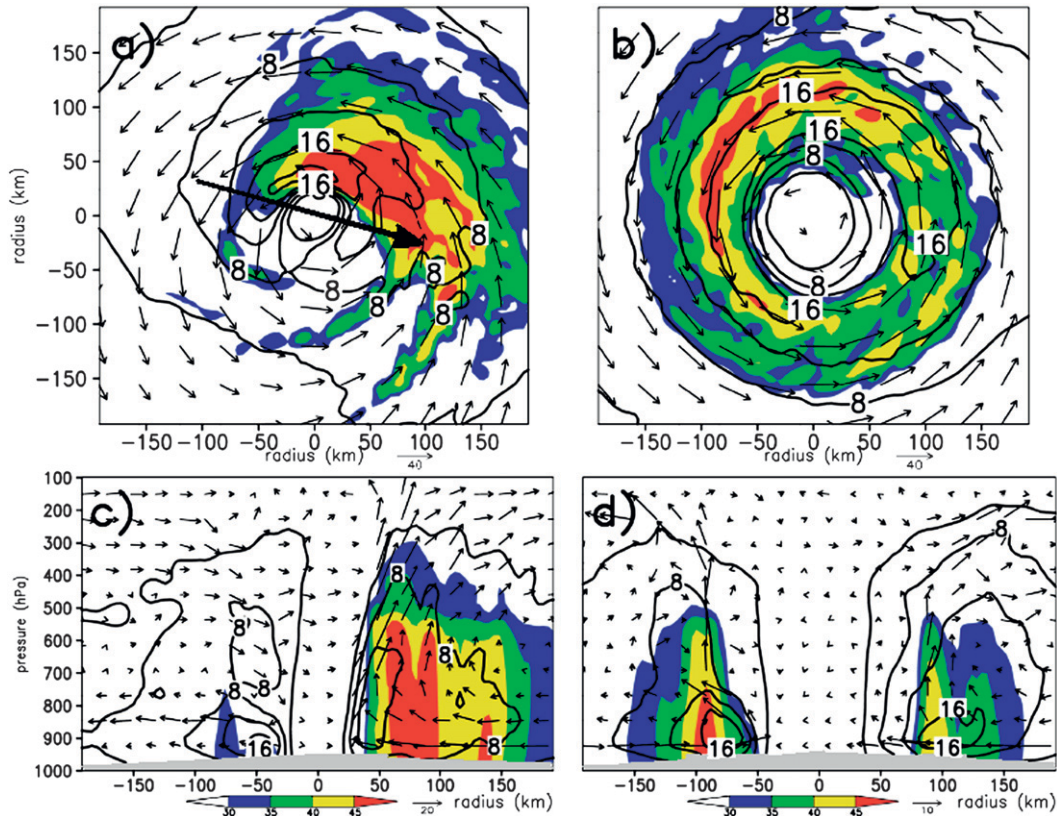


FIG. 2. (a),(b) Horizontal distribution of KE, contoured at intervals of $4 \times 10^2 \text{ J kg}^{-1}$, and radar reflectivity (shaded) at 900 hPa averaged during (a) the 46–47-h and (b) the 96–97-h simulations; (c),(d) the corresponding west–east vertical cross sections through the storm center. In-plane flow vectors are superposed. The thick arrow in (a) denotes the vertical shear vector in the 850–200-hPa layer.

volume, and the other variables assume their typical meteorological definition. The vertical component of KE, $w^2/2$, is excluded because it is one to two orders of magnitude smaller than the horizontal component.

We start from a prognostic equation for LE, which is essentially the available water vapor contained in the atmosphere, to account for the most crucial component for TC development and maintenance. It is obtained by multiplying the water vapor budget equation from Zhang et al. (2002) by the latent heat of vaporization, L_v :

$$\frac{d}{dt}(\text{LE}) = -\rho L_v(Q_{\text{con}} - Q_{\text{ev}}) + \text{LHF} + \text{LE} \frac{d \ln \rho}{dt}, \quad (1)$$

where the three rhs terms represent sources and sinks of LE due to condensation and evaporation (LHR), the evaporative source of vapor fluxes from the ocean surface (LHF), and the condensing or dilution of LE due to density changes (LDEN). The final term arises from the inclusion of density in the definition of LE. Note that the density changes can be estimated as negative 3D velocity divergence through the mass continuity equation.

For the sake of energy conversion analysis, $L_v(Q_{\text{con}} - Q_{\text{ev}})$ is approximated by the net heating rate, $c_p/\pi d\theta/dt$, where $\pi = (p_0/p)^{R/c_p}$, θ is the potential temperature, R is the universal gas constant, and $d\theta/dt \approx (\mathbf{V} - \mathbf{U}) \cdot \nabla \theta$, where \mathbf{U} is the horizontal storm motion vector and the del operator is the 3D gradient. This approximation for heating introduces errors such as those due to radiation and the local θ tendency resulting from the internal dynamics, but the latter was found by Zhang et al. (2002) to be small (see their Figs. 3 and 5).

While the latent heating rates can serve as a proxy for the LE consumed in deep convection, the same term appears, but with an opposite sign, in the TPE equation, which can be obtained directly from the MM5 thermodynamic equation:

$$\begin{aligned} \frac{d}{dt}(\text{TPE}) = & -\nabla \cdot (p\mathbf{V}) + \mathbf{V}_H \cdot \nabla p' + \rho L_v(Q_{\text{con}} - Q_{\text{ev}}) \\ & + \text{SHF} + \text{TPE} \frac{d \ln \rho}{dt}, \end{aligned} \quad (2)$$

where the five terms on the rhs represent the sources and sinks of TPE due to the convergence of pressure, the

TABLE 1. Symbols and units of energetic quantities used in this study.

Symbol	Description	Units
$B\bar{K}$	Azimuthally averaged BKE	J m^{-3}
BK'	Perturbation BKE	J m^{-3}
BKE	Volume-averaged KE	J m^{-3}
BLE	Volume-averaged LE	J m^{-3}
BTPE	Volume-averaged TPE	J m^{-3}
KDEN	KE changes due to density changes	W m^{-3}
KDIS	KE dissipation	W m^{-3}
KE	Kinetic energy	J m^{-3}
KFLX	BKE changes due to boundary flux divergence	W m^{-3}
KGEN, $C(\text{TPE}, \text{KE})$	KE generation	W m^{-3}
LDEN	LE changes due to density changes	W m^{-3}
LFLX	BLE changes due to boundary flux divergence	W m^{-3}
LE	Latent energy	J m^{-3}
LHF	Latent heat flux (ocean)	W m^{-3}
LHR, $C(\text{LE}, \text{TPE})$	Latent heat release	W m^{-3}
TPE	Total potential energy	J m^{-3}

horizontal cross-isobaric flow (p' denotes the deviation from the hydrostatic base-state pressure), the latent heating rate, sensible heat fluxes from the ocean surface, and the condensing or dilution of TPE due to density changes. For the purposes of this study, we will consider TPE to be simply the intermediary between LE and KE, both of which will be the focus of the present study.

The KE equation can be obtained by taking the dot product of the MM5 horizontal momentum equation:

$$\frac{d}{dt}(\text{KE}) = -\mathbf{V}_H \cdot \nabla p' - \mathbf{V}_H \cdot \mathbf{F} + \text{KE} \frac{d \ln p}{dt}, \quad (3)$$

where KE changes because of horizontal cross-isobaric flow when work is done by air parcels against the horizontal pressure force (KGEN), friction including the boundary layer processes and vertical and horizontal diffusion (KDIS), and the condensing or dilution of KE due to density changes (KDEN).

The intensification and maintenance of a TC can be described as a series of energy conversions that occur primarily within its secondary circulations. As moist air is drawn from the planetary boundary layer (PBL) upward and condensed into liquid water, latent heat is released in exchange for water vapor. In this way, LE is converted to TPE through latent heating; that is, $C(\text{LE}, \text{TPE}) = \rho L_v (Q_{\text{con}} - Q_{\text{ev}})$. The midtropospheric warming causes pressure drops below, leading to increases in the pressure gradient force. As a result, KE must increase, and it does so at the expense of TPE via adiabatic cross-isobaric flow to regain gradient balance. Thus, KE is produced through conversion from TPE; that is, $C(\text{TPE}, \text{KE}) = -\mathbf{V}_H \cdot \nabla p'$, and TPE is the intermediary between KE and LE.

4. Volume-integrated energetics

Although Eqs. (1)–(3) are useful for estimating the spatial structures of TC energetics, it would be more appropriate to use the area- or volume-averaged budgets that could distinguish internal sources/sinks from the lateral boundary fluxes, especially when the time evolution of the storm-scale integrated quantities in a storm-relative framework is examined. For this purpose, we define a control cylindrical volume of $R = 200$ km and $z = 15$ km, centered at the minimum surface pressure, following the movement of Bonnie at 15-min intervals during the 36–96-h integration. The volume-integrated form of Eqs. (1)–(3) can be written using (Dutton 1976)

$$\begin{aligned} \frac{d}{dt} \left[\int_{V(t)} \alpha dV \right] &= \int_{V(t)} \frac{\partial \alpha}{\partial t} dV + \int_S \alpha \mathbf{U} \cdot \mathbf{n} dS \\ &= \int_{V(t)} E_s dV + \int_S \alpha (\mathbf{U} - \mathbf{V}) \cdot \mathbf{n} dS, \quad (4) \end{aligned}$$

where α denotes LE, KE, and TPE; E_s is the energy sources minus sinks (i.e., the rhs terms of each energy equation); S represents the two-dimensional surface that laterally bounds the control volume; and \mathbf{U} represents the horizontal translation velocity of the control volume. The last rhs term represents the energy flux divergence at the lateral boundaries. To distinguish from their differential forms, we refer to the volume-integrated energies as bulk energetics (i.e., BLE, BKE, and BTPE). In addition, a volume average has been implicitly assumed for the bulk energies as well as for their budget terms. By combining Eq. (4) with Eqs. (1) and (3), and after some manipulation, the volume-integrated

forms of the budget equations for BKE and BLE are obtained:

$$\frac{d}{dt} \text{BKE} = - \int \mathbf{V}_H \cdot \nabla p' dV - \int \mathbf{V}_H \cdot \mathbf{F} dV - \int \nabla \cdot \text{KE}(\mathbf{V} - \mathbf{U}) dV, \quad \text{and} \quad (5)$$

$$\frac{d}{dt} \text{BLE} = - \int \rho L_V (Q_{\text{con}} - Q_{\text{ev}}) dV - \int \text{LHF} dV - \int \nabla \cdot \text{LE}(\mathbf{V} - \mathbf{U}) dV, \quad (6)$$

where the symbols take on the previously defined meanings. The flux divergence terms on the rhs of Eqs. (5) and (6) are hereafter referred to as KFLX and LFLX. To make sure that the budget residues are small, we have compared the energy changes calculated from the lhs terms of Eqs. (5) and (6) to those obtained by summing the rhs forcing terms during the study period and have found that the differences between the two approaches are small (not shown).

The evolution of bulk energetics allowing lateral boundary fluxes is given in Fig. 3a, which shows pronounced variations in magnitude for both BLE and BKE. The net BKE increases by about 60% during the rapid deepening phase and remains nearly constant until 60 h, after which the BKE increases by another 20% between 60 and 66 h. Then it decreases by about 15% between 66 and 81 h, during which period the eyewall replacement begins with the decay of the partial eyewall and increases subsequently after 81 h, when the new axisymmetric eyewall organizes and contracts. Its total net increase is about 120% in 60 h. The BKE changes coincide reasonably well with the intensity changes (cf. Figs. 3a and 1), but differences between the time series indicate that BKE could be used as a unique indicator of hurricane intensity (Powell and Reinhold 2007).

The trend in BLE is much less drastic than that of BKE, with a maximum decrease of 7% at the peak intensity and a net 1% increase at the end of the 96-h integration. The BLE decrease during the 36–65-h simulation corresponds to the rapid deepening phase with increasing BKE, suggesting the rapid consumption of water vapor by deep convection in the eyewall. Of interest is that BLE shifts to a positive trend after 66 h (i.e., at the end of the maintenance phase of the storm). At the same time, BKE also begins to decrease as the eyewall replacement cycle begins.

The storm-integrated BTPE is one order of magnitude larger than BLE and three orders of magnitude larger than BKE, and it decreases by only about 2% throughout the integration. A close inspection of Fig. 3a reveals that

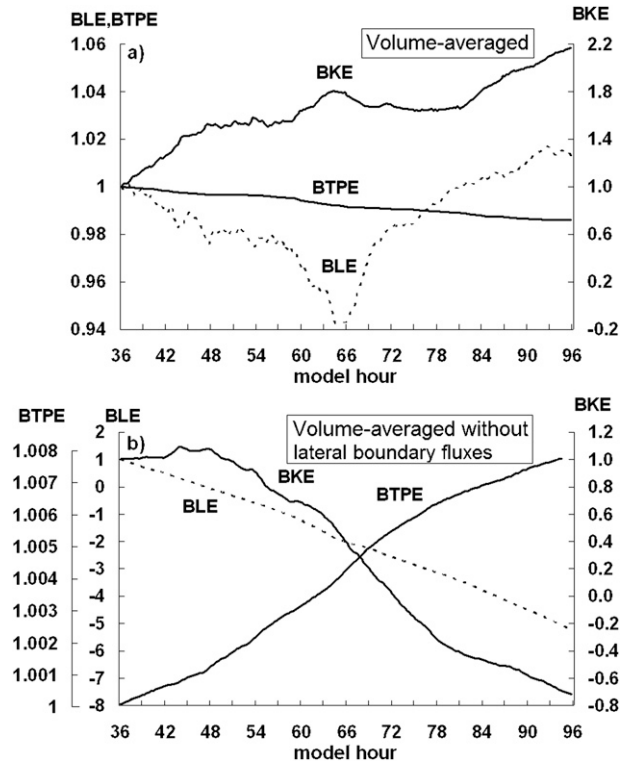


FIG. 3. Time series (15 min) of the volume-averaged (a) BKE (right ordinate), BLE, and BTPE (left ordinate) following the storm; and (b) their corresponding evolution without the lateral boundary fluxes. Each time series has been normalized such that each 0.01 represents a 1% change from the initial value of the energy, that is, 1.28×10^2 (BKE), 7.89×10^3 (BLE), and $9.92 \times 10^4 \text{ J m}^{-3}$ (BTPE).

the rate of BKE increase is roughly correlated to the rate of BTPE decrease. This suggests that when Bonnie is intensifying, BKE increases at the expense of BTPE. Cross-isobaric flows are the only physical connection between BKE and BTPE, as described by Eqs. (2) and (3), and will be further discussed in the next section.

Note that the above results are presented in an open system. The evolution of bulk energetics without the lateral boundary fluxes, given in Fig. 3b, shows quite different trends from those shown in Fig. 3a, drawing attention to the importance of lateral energy fluxes. That is, the evolutionary trends for all the bulk energetics are opposite to their counterparts after removing the lateral fluxes, except for BLE during the initial deepening stage. The net BLE decreases by over 500%, indicating that the BLE source from the ocean in the immediate storm vicinity alone (i.e., without the far-field contribution) is inadequate to compensate for the rapid consumption of LE via LHR. BKE also decreases continuously in the absence of lateral fluxes due to the dissipation of KE in the PBL, as will be seen in the next section. Figure 3b

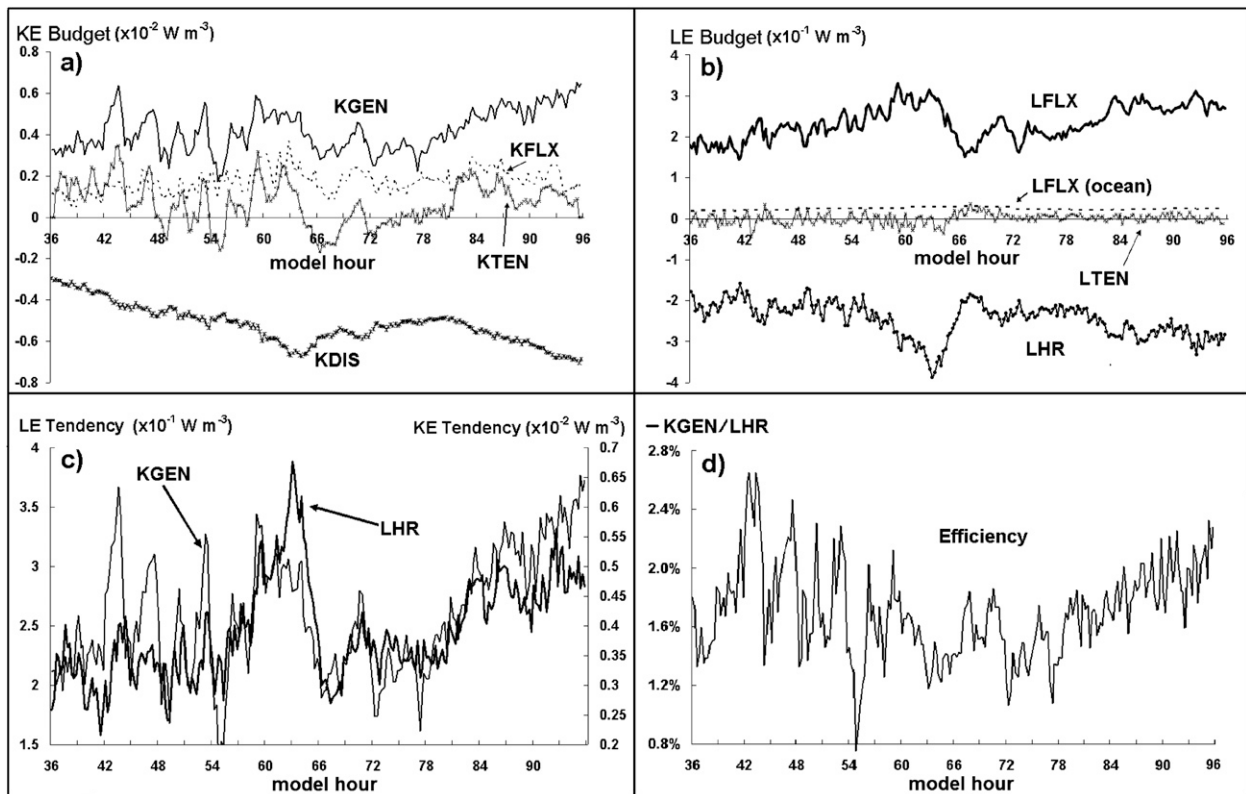


FIG. 4. Time series (15 min) of the volume-averaged (a) BKE and (b) BLE tendency (both in W m^{-3}) and their budgets, following the storm. (c) A comparison of LHR (with sign reversed) with KGEN, with a correlation coefficient of 0.65, and (d) the efficiency of KGEN.

also shows negative energies for both KE and LE at the later stages because more inward than outward lateral energy fluxes occur, especially for LE. On the other hand, BTPE increases, albeit by less than 1%, implying that the sensible heat, converted from latent heat in the storm, is transported away from the storm across the lateral boundaries.

The budget calculations in Fig. 4 clarify the above-mentioned processes and emphasize that lateral energy fluxes are critical for TC development. It is obvious from Fig. 4 that there are pronounced offsets between the PBL friction (KDIS) and BKE production (KGEN; Fig. 4a), and between convective consumption (LHR) and moisture supply (LFLX) through the lateral boundaries (Fig. 4b). In general, the budget terms increase in magnitude slowly prior to 63 h, although the BKE production (KGEN) is highly variable during the partial eyewall stage. As will be shown in section 6, the large BKE tendency fluctuations (during the 42–60-h period) are attributable to the growth and decay of inner-core convection, which produces intense cross-isobaric flows in the PBL. Figure 4c shows that the time series of KGEN is in phase with that of LHR, including their fluctuations during the 42–60-h period and sharp changes during the

63–66-h period. The close correspondence between LHR and KGEN provides further evidence that the fluctuations in the time series must be related to convection and are not numerical noise. In contrast to the large fluctuations in KGEN, the frictional dissipation of BKE is relatively smooth, following closely the time series of BKE (cf. Figs. 4a and 3a). The primary difference between the KGEN and KDIS time series is that KGEN occurs only with cross-isobaric flows, whereas KDIS acts to dissipate all BKE, most of which occurs through the more slowly varying balanced flows. The flux divergence of the storm BKE (KFLX) evolves steadily at a near-constant rate of $2 \times 10^{-3} \text{ W m}^{-3}$ throughout the lifetime of Bonnie, indicating a net import of BKE through the lateral boundaries, likely in the PBL.

Figure 4b shows increasing moisture supply through the lateral boundaries and moisture consumption until 63 h; the latter occurs more rapidly during 54–63 h, a period that coincides with a negative BLE and positive BKE tendency (Fig. 4c). Of interest is that the moisture consumption through LHR and moisture supply through LFLX decrease rapidly after 63 h, a time when Bonnie's partial eyewall begins to rapidly decay and BKE begins to decrease (cf. Figs. 4 and 3a). At this time, the moisture

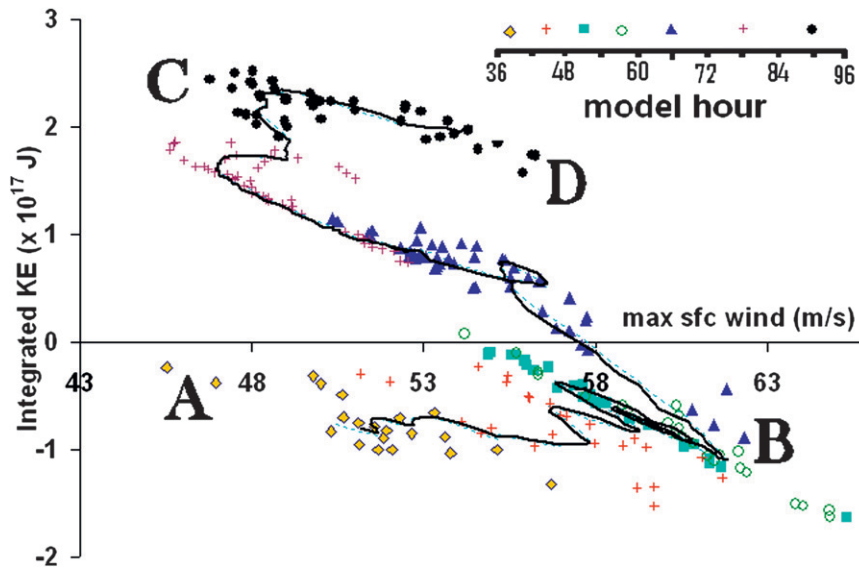


FIG. 5. Phase diagram relating the maximum surface wind and BKE deviation during the 36–96-h simulation, plotted every 15 min using various types of symbols, beginning with filled diamonds (36–42 h) and ending with filled circles (84–96 h). The BKE deviation is calculated from an observed mean KE for a given intensity. The solid line is a 10-point moving average. Labels A, B, C, and D represent characteristic stages of Bonnie’s development, as discussed in the text.

consumption decreases more than the moisture supply, which is consistent with the positive tendency of BLE and negative tendency of BKE during 66–69 h (cf. Figs. 4b and 3). This period can be considered a time of moisture replenishment, as the partial eyewall and associated BLE consumption diminish. After 72 h, both the moisture consumption and supply rates increase slowly as Bonnie reorganizes into axisymmetry. Note that the moisture supply from the lateral boundaries is an order of magnitude larger than that from the ocean surface. Although the surface moisture flux contributes a small amount of BLE within the $R = 200$ km integration domain, the storm would not intensify without it or at the reduced amount (see Zhu and Zhang 2006b), suggesting the importance of surface moisture fluxes occurring at a much larger scale. In general, the BLE budget is in delicate balance, with the BLE tendency (LTEN; Fig. 4b) representing a small difference between two large terms, LFLX and LHR, and a small contribution from the ocean flux at the storm scale.

Although the evolution of BKE coincides generally well with that of the minimum central pressure and maximum surface wind (V_{MAX}), the correspondence is not exact. One novel way to address the relationship between BKE and V_{MAX} has been set forth by Maclay et al. (2008), who created phase diagrams describing BKE deviations as a function of V_{MAX} for various observed storms. That is, for a given V_{MAX} , the BKE de-

viation is calculated in reference to an expected value of BKE that is estimated as the best fit from the observed data of multiple storms. A storm with a negative or positive BKE deviation at any moment could be considered as being bulk-energetically small or large, respectively. For example, the record-breaking Hurricane Wilma (2005) with a smaller RMW at its maximum intensity and Katrina (2005) with a larger RMW near landfall are extreme examples of storms with negative and positive KE deviations, respectively.

A phase diagram for the simulated Bonnie, following Maclay et al. (2008), is given in Fig. 5, which shows that Bonnie is both bulk-energetically small and large but at different stages. That is, Bonnie exhibits a negative BKE deviation during the 36–63-h period (i.e., from A to B in Fig. 5), indicating that the storm contains less BKE than would be expected for a storm of similar intensity due to its partial eyewall with a relatively small RMW (i.e., 50 km). The phase diagram exhibits diagonal fluctuations during 42–60 h due to the fluctuations in V_{MAX} shown in Fig. 1. Subsequently after 63 h (B to C in Fig. 5), the BKE deviation becomes positive and continues to increase until near 84 h, suggesting that Bonnie is bulk-energetically growing during the 63–84-h period, even though V_{MAX} decreases as the partial eyewall decays. Meanwhile, an outer eyewall begins to organize, leading to a new RMW located near 100 km. This eyewall replacement is consistent with the bulk energetic

growth that begins near hour 66 and ends near hour 84. Between 84 and 96 h (C to D in Fig. 5), the BKE deviation decreases once again, suggesting a decrease in the bulk-energetic size of Bonnie. In fact, as shown in Part I, this period is characterized by the contraction of the axisymmetric eyewall.

In this regard, the phase diagram provides a 3D description of the evolution of Bonnie in terms of the storm size, intensity, and development stage. The phase transitions are relatively smooth throughout most of the evolution, except for the 42–60-h period during which Bonnie exhibits rapid diagonal oscillations every few hours (Fig. 5). Each oscillation gives the appearance of a “horizontal question mark,” as suggested by Maclay et al. (2008), and represents alternating intensification and bulk-energetic shrinking (down to the right) and weakening and bulk-energetic growth (up to the left). This behavior is associated with organized convective processes in the eyewall that will be discussed in the next section. Such a close correspondence of the horizontal question mark shape between the observation-based study of Maclay et al. and the results here (Fig. 5) encourage further confidence in the realism of the present simulation of Bonnie.

5. Energy conversions

LHR and KGEN are the two primary energy conversion processes—that is, $C(\text{LE}, \text{TPE})$ and $C(\text{TPE}, \text{KE})$ represent the main route of energy from LE to KE, and they are highly correlated (Fig. 4c). However, on average only about 1.8% of LHR could be converted to KE through KGEN (Fig. 4d), while the remainder is used to heat the atmosphere. In this sense, the hurricane is thermodynamically inefficient. Large fluctuations in the thermodynamic efficiency, varying from 0.8% to 2.6%, occur during the partial eyewall stage through KGEN because of the large oscillations in cross-isobaric flows to be discussed later in the context of VRWs. Note that the mean efficiency remains above 1.6%, except during 63–78 h, during which period the bulk energetic size of Bonnie is increasing (cf. Figs. 4d and 5) but BKE is decreasing (cf. Figs. 4d and 3a). This implies that when Bonnie is weakening and bulk-energetically growing, it is least efficient in converting LE to KE. On the contrary, when BKE is increasing most rapidly, efficiency increases, due partly to the increased KE and partly to the reduced RMW (Hack and Schubert 1986).

Figure 6 shows that $C(\text{LE}, \text{TPE})$ and $C(\text{TPE}, \text{KE})$ are also horizontally well correlated. For example, during the partial eyewall stage, the shear-induced vertical circulation, as described by Black et al. (2002) and Zhang and Kieu (2006), dictates the distribution of LHR, with higher

magnitudes on the downshear left and little in the southwestern quadrant of the eyewall (Fig. 2a). Thus, both $C(\text{LE}, \text{TPE})$ and $C(\text{TPE}, \text{KE})$ are peaked in the northeastern quadrant where the friction-induced convergence is maximized (Fig. 6a). In the vertical, $C(\text{TPE}, \text{KE})$ is peaked at the surface in the eastern half (Fig. 6c), and it becomes negative in the supergradient outflows aloft (see Zhang et al. 2001).

However, the energy conversion to KE is negative in the lowest 300 hPa and positive aloft in the western half (Fig. 6c) because of the presence of vertically distributed radial flows that are opposite to those in the eastern half. This vertical structure appears to be typical under the influence of strong vertical shear. That is, the strong inflow aloft descends isentropically on the upshear side of the eyewall, and the resulting increase in the tangential flow as a result of the angular momentum conservation may cause the centrifugal force to exceed the local radial pressure gradient force, leading to the supergradient consumption of KE near the inner eyewall edge (Fig. 6c). On the other hand, the KE destruction in the lowest 300-hPa layer does not seem to be associated with the supergradient outflow jet, as discussed in Zhang et al. (2001). Our analysis reveals that it is associated with evaporatively driven outflows from moist downdrafts that are induced on the upshear side, as precipitation particles advect cyclonically in the eyewall and then encounter a dry intrusion in the 550–800-hPa minimum θ_e layer (cf. Figs. 6c and 7). As discussed in Kieu and Zhang (2008), the generation of moist downdrafts in the minimum θ_e layer represents the thermodynamic impact of vertical wind shear. The moist downdrafts could eventually reach the surface and generate locally higher pressures to reverse the mean pressure gradients in the PBL such that the descending flows could be forced outward (Fig. 7). Such an outflow has also been observed by Black and Holland (1995) in Hurricane Kerry (1979), which developed in a strong sheared environment. They attributed this outflow to a combination of surface processes and environmental shear.

After the transition to axisymmetry, Bonnie exhibits more symmetric LHR and KGEN in both the horizontal (Fig. 6b) and vertical (Fig. 6d), only with a slight asymmetric circulation in the eye. Although LHR occurs throughout the eyewall, positive KGEN appears mostly over a broad region in the lowest 100-hPa layer with the peak near the RMW. Positive KGEN appears also near the melting level where secondary convergence occurs. Note the KE consumption in the low-level eye (Fig. 6b) due to the presence of divergent flows associated with the supergradient outflows above (see Liu et al. 1997; Zhang et al. 2001). This indicates that moist air is drawn from the eye, against the pressure gradient force, into

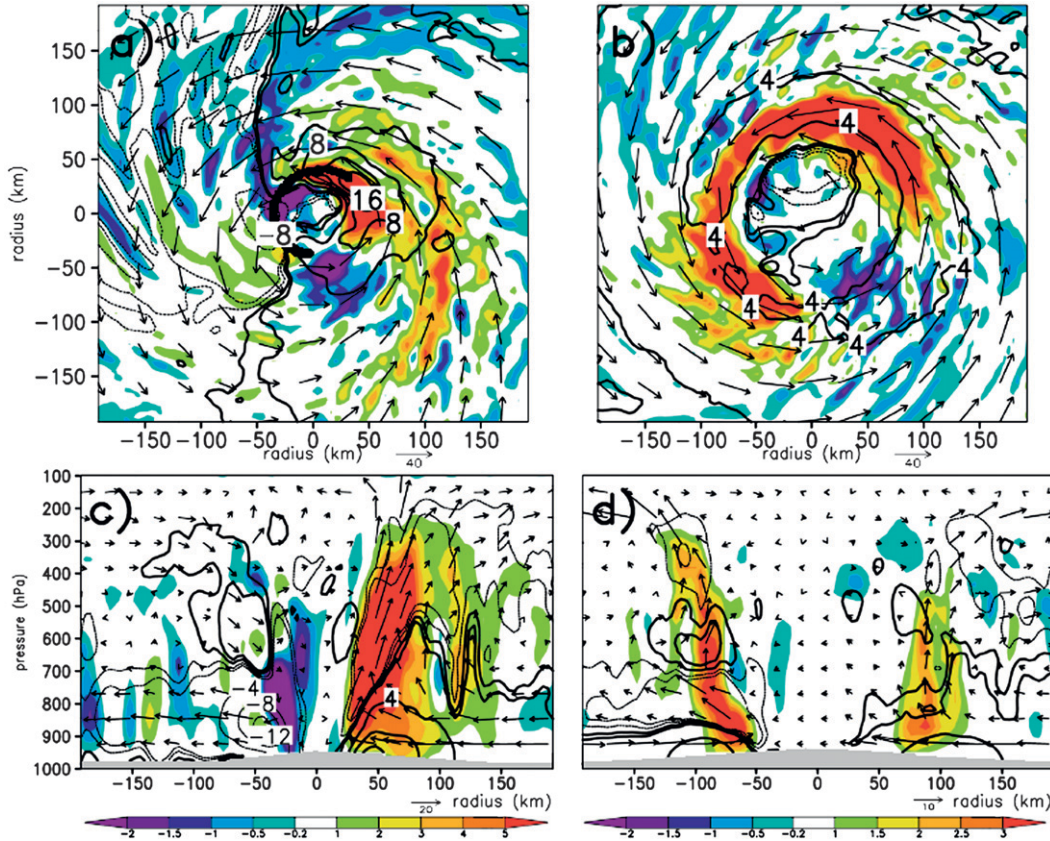


FIG. 6. As in Fig. 2, but for KGEN contoured at intervals of $4 \times 10^{-1} \text{ W kg}^{-1}$ for magnitudes greater than $\pm 4 \times 10^{-1} \text{ W kg}^{-1}$ and otherwise at values of 0.5, 0.2, -0.2 and $-0.5 \times 10^{-1} \text{ W kg}^{-1}$; heavy (light) contours are for positive (negative) KGEN. Latent heat release is shaded according to the color bar in units of W kg^{-1} . The heavy arc in (a) denotes the location of the cross section in Fig. 7.

the eyewall. LHR is negative at the eye–eyewall interface (Fig. 6d), indicative of evaporative cooling.

6. Eddy KE, VRWs, and intensity change

Because VRWs may be closely related to the development of eddy KE (Wang 2002a), it is desirable to decompose KE into the azimuthal mean (\bar{K}) and eddy (K') components to gain insight into the relationship between VRWs and hurricane intensity changes. For this purpose, we decompose $\text{KE} = \rho(\bar{K} + K')$, $\bar{K} = (U^2 + V^2)/2$ and $K' = (u'^2 + v'^2)/2$, where $U(V)$ and $u'(v')$ are the azimuthal mean and deviation from the mean of the radial (tangential) wind, respectively. Note that the air density, ρ , is not decomposed. We will use $B\bar{K}$ and BK' below to denote the volume-averaged mean and perturbation KE, respectively.

Figure 8 shows that most of BKE is contained in $B\bar{K}$, and BK' is one order of magnitude smaller than $B\bar{K}$. Of importance is that the evolution of BK' is highly positively correlated with that of vertical shear; that is, as

the vertical shear increases from 12 to 19 m s^{-1} , BK' amplifies from 10 to 30 J m^{-3} , corresponding to large asymmetries in deep convection and horizontal winds (Fig. 2a). Of further importance is that the most rapid increase (decrease) in BK' occurs when the vertical shear exceeds (falls below) 12 m s^{-1} [e.g., near 40 h (65 h)]. Prior to and after this threshold, BK' remains small, and thus Bonnie can be characterized as near-axisymmetric.

The radius–height structures of \bar{K} and K' are given in Fig. 9, which shows that during the partial eyewall stage K' is maximized in the PBL with a peak value of more than 250 J kg^{-1} near the eye–eyewall interface (Fig. 9a). In this sense, the surface winds could indeed be used to characterize the asymmetry of horizontal winds. The magnitude of K' decays both vertically and radially, but with a secondary maximum in the upper outflow layer, which is similar to the idealized numerical study of Wang (2002a). Because the peak K' occurs below the maximum LHR and is collocated roughly with the maximum KGEN (cf. Figs. 6a and 9a), the mechanisms (e.g., VRWs), to be later examined, by which large K'

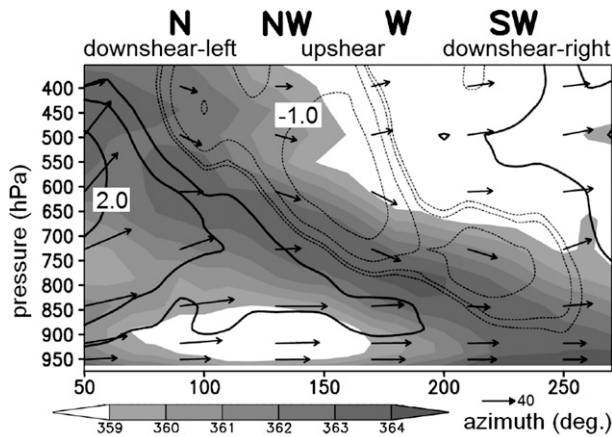


FIG. 7. Pressure–azimuth cross section of equivalent potential temperature θ_e (shaded), vertical motion [contoured as thick (thin) lines for positive (negative) values at -1.0 , -0.5 , -0.2 , -0.1 , 0.5 , 1.0 , 2.0 , 4.0 , and 8.0 m s^{-1}], and in-plane flow vectors that are taken at $R = 40 \text{ km}$ and averaged during the 46–47-h simulation (see Fig. 6a for the location). Note the descending motion that extends to the PBL in the western half of the storm.

is generated must play an important role in Bonnie's intensity changes. In contrast, during the symmetric stage, Fig. 9b shows that the values of \overline{K} (K') are larger (smaller) than those at the asymmetric stage. In general, the magnitude of K' is about $1/3$ to $1/4$ of that at the earlier stage, suggesting different mechanisms or perturbation structures in the case of weak vertical shear.

Before examining the relationship between the perturbation structures and intensity changes, we first take a look at the relative significance of different wavenumber components (e.g., wavenumbers 1 and 2, hereafter WN-1, and WN-2) in determining the magnitude of K' (Fig. 10a). Because K' is peaked in the PBL, its wavenumber decomposition will be performed for the lowest 3 km. Apparently, the wavenumber-0 (hereafter WN-0) component (i.e., \overline{BK} in Fig. 8a) of the low-level KE is one order of magnitude larger than either of the next two components, WN-1 and WN-2, which together represent most of the K' . Note that the WN-1 KE is larger than WN-2 until 78 h (Fig. 10a), after which the two components are nearly equal as the vertical shear decreases below 12 m s^{-1} . This is consistent with our intuition that all nonzero wave components should be small and nearly equal under the influence of weak vertical shear.

In contrast to the dominant WN-0 KE, the vertical motion is dominated by WN-1 during the 36–72-h period (Fig. 10b), thus agreeing with previous studies about the importance of vertical shear in determining the cloud asymmetries during the partial eyewall stage. All components of vertical motion exhibit significant fluctuations

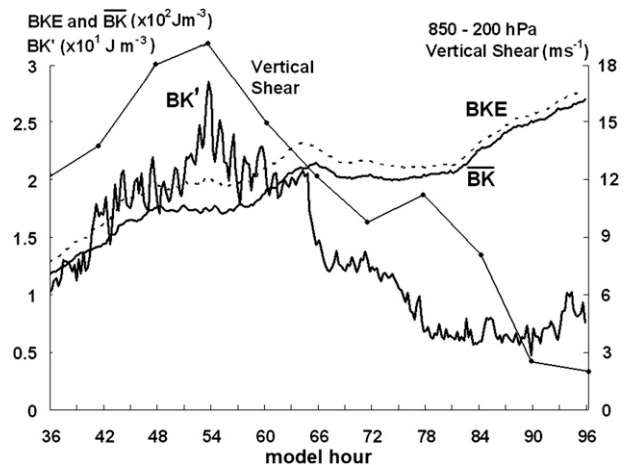


FIG. 8. Time series (15 min) of the volume-averaged BKE (dashed), \overline{BK} (solid), and BK' (solid) scaled in the left ordinate for a cylindrical volume with $R = 200 \text{ km}$ and $Z = 15 \text{ km}$. Area-averaged 850–200-hPa vertical shear (thin solid; right ordinate) from Part I is shown every 6 h.

tuations between 42–60 h, which are well correlated to those in the KE production and the maximum wind speed, with peaks at model hours 43, 47, 50, 53, 57, and 60 (cf. Figs. 10b, 5c, and 1). The amplitude of WN-1 vertical motion diminishes and becomes nearly equal to that of WN-0 and WN-2 as the vertical shear weakens to less than 12 m s^{-1} after 63 h, at which time the partial eyewall begins to break down. After the rapid decay of the WN-1 vertical motion near 63 h, the WN-0 vertical motion slowly grows, and after 87 h, WN-0 becomes dominant as the secondary eyewall organizes and contracts.

In the next subsections we attempt to show for the above two different stages that (i) the intensity fluctuations coincide closely with the azimuthal propagation of VRWs and deep convection in the eyewall and (ii) the eyewall replacement occurs as a result of the outward propagation of VRWs and deep convection.

a. The partial eyewall stage

Figure 11 presents the evolution of vertical motion, used as a proxy for LHR, at 30-min intervals during a characteristic fluctuating period (i.e., 44–48 h into the simulation), during which the maximum surface wind decreases from 60 to 55 m s^{-1} during the 42–45-h period, then increases to 63 m s^{-1} by 47 h, and decreases again to 55 m s^{-1} by 48 h (see Fig. 1). The first period of weakening winds coincides with the decay of eyewall convection (Fig. 11, top), and at 45.5 h a single convective element, denoted A_1 , initiates in the southeast quadrant of the storm near the RMW ($R = 50 \text{ km}$). Thus, KGEN associated with the convective element will act to

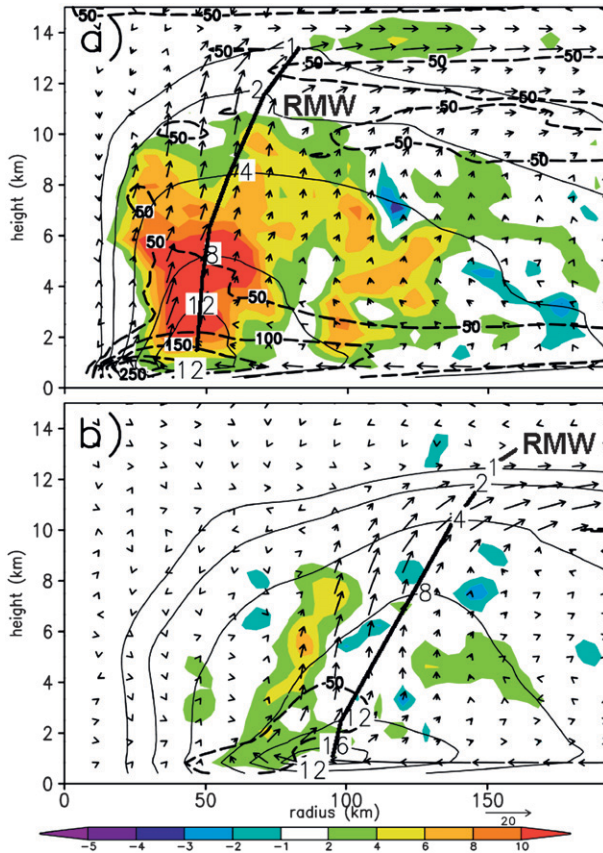


FIG. 9. Height–radius cross sections of \bar{K} (thin solid contours at values of 1, 2, 4, 8, 12, and $16 \times 10^2 \text{ J kg}^{-1}$), K' (dark dashed contours at intervals of 50 J kg^{-1}), and azimuthal mean latent heat release (shaded) in units of W kg^{-1} averaged during the (a) 46–47-h and (b) 96–97-h simulations. The azimuthally averaged in-plane flow vectors and the vertical axis of the RMW are superposed.

accelerate surface winds near the RMW. The element intensifies as it propagates cyclonically toward the northeastern quadrant, where a favorable shear-induced upward motion is present, and reaches peak intensity near 47 h (denoted A_2), when the eastern half of the storm is almost entirely filled with deep convection. By 48 h, deep convection, now denoted A_3 , begins to decay as it moves into the unfavorable upshear side of the hurricane vortex. This convective evolution in the eyewall corresponds well to the fluctuations of the maximum surface wind (cf. Figs. 1 and 11); the other fluctuating periods shown in Fig. 1 correspond similarly well. Because convective elements cannot propagate around the eyewall under the constraint of vertical shear, Bonnie’s intensity fluctuates in response to the life cycle of shear-forced convective elements, which grow (dissipate) on the downshear (upshear) side.

Qualitatively, the azimuthal and outward propagation of the spiral band in Fig. 11 resembles the evolution of

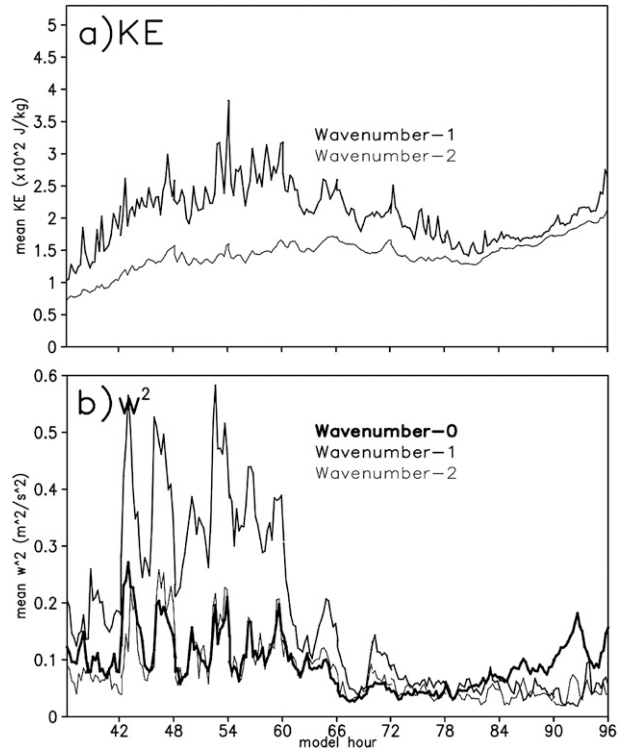


FIG. 10. Time series (15 min) of the area-averaged ($r = 200 \text{ km}$) Fourier decomposition of (a) KE averaged in the 0–3-km layer and (b) the vertical motion averaged in the 6–10-km layer.

VRWs as proposed by Montgomery and Kallenbach (1997) and discussed as a result of the breakdown of an annular ring of vorticity by Kossin et al. (2000). To help gain insight into the above propagation characteristics, the time evolution of the WN-1 and WN-2 vertical motion and their associated low-level pressure fields are examined during the above period, since the two wave components account for much of the vertical motion and KE fluctuations (see Fig. 10). Additionally, one can see from Fig. 12a that the vertical shear sets up a standing WN-1 wave of the vertical motion with a low-level inflow (outflow) and positive (negative) vertical motion on the downshear (upshear) side of the vortex. By comparison, the WN-2 fields during the partial eyewall stage exhibit robust structures with the pressure and vertical motion well coupled near the RMW at $R = 60 \text{ km}$. The sum of the WN-1 and WN-2 components captures well the structure of the convective element as it evolves between A_1 and A_2 in the southeast quadrant of the storm (cf. Figs. 11 and 12a), whose growth during this hour coincides with a rapid increase in the maximum surface wind, as well as the simultaneous cyclonic and outward propagation during the subsequent hours.

The detailed evolution of the pressure and vertical motion at WN-2 is given in Fig. 13a, which shows

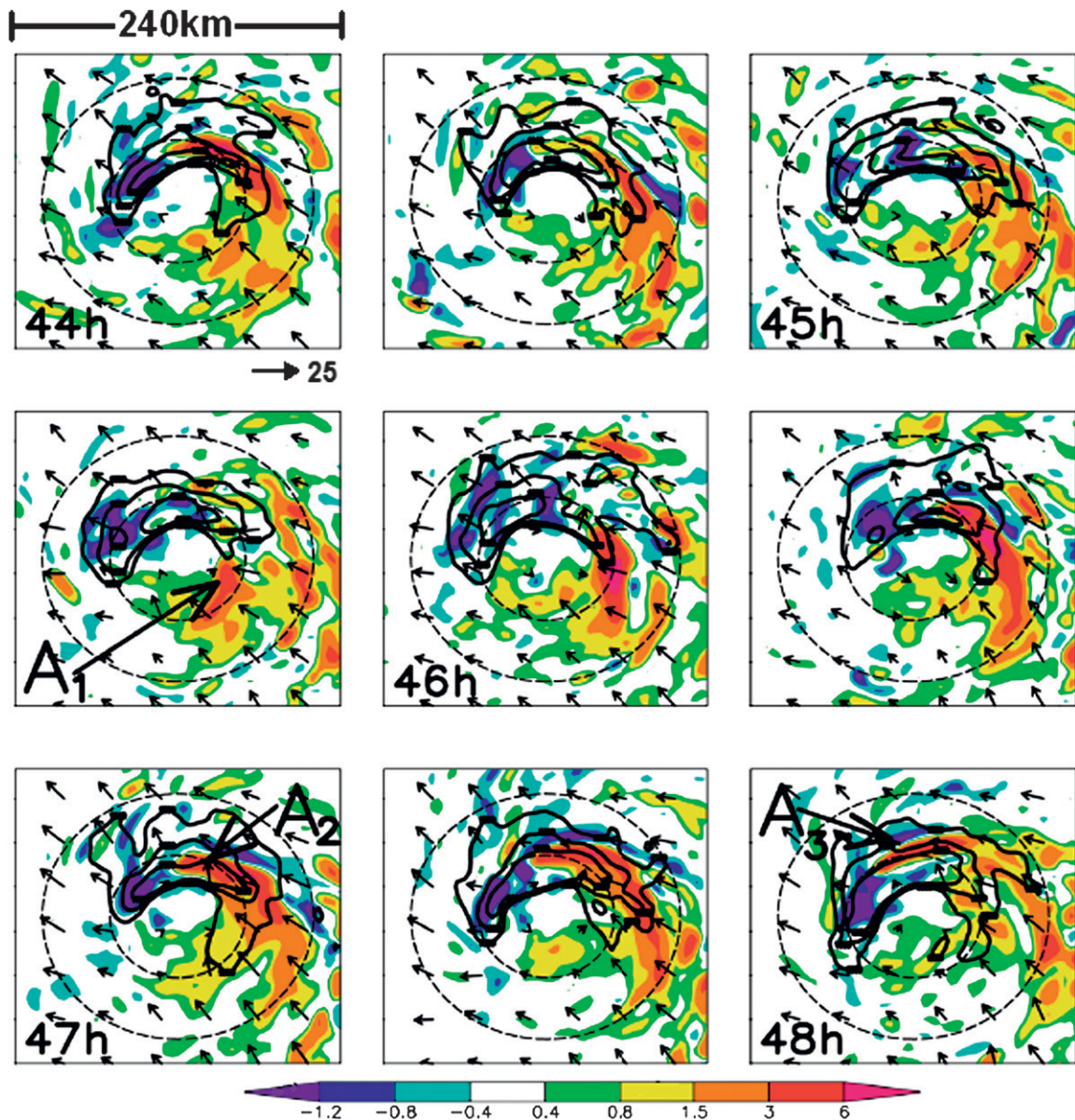


FIG. 11. Horizontal distribution of the averaged KE in the lowest 3-km layer (contoured at values of 13 , 16 , and $19 \times 10^2 \text{ J kg}^{-1}$) and the averaged vertical motion in the 6–10-km layer (shaded) from the 44–48-h simulation. Horizontal asymmetric flow vectors at $z = 1.5 \text{ km}$ are superimposed. Dashed circles represent radius rings at $R = 50 \text{ km}$ and $R = 100 \text{ km}$; A_1 , A_2 , and A_3 denote the respective initiation, maturation, and decay of a single convective element.

that the convective element responsible for the intensity fluctuation is initiated at the leading edge of a cyclonically propagating WN-2 low pressure perturbation at 45.5 h. This low pressure center is seen propagating one full circle at $R = 50 \text{ km}$ during 44.5–47 h and exhibiting a speed of 35 m s^{-1} , which is roughly 73% of the mean tangential wind speed. However, the associated WN-2 vertical motion perturbation fails to make a complete circle: it is initiated near the location of maximum radial PV gradient and propagates radially

down the PV gradient at a speed of 7 m s^{-1} (cf. Figs. 13b,c). The azimuthal and radial speeds are consistent with VRWs as observed (Corbosiero et al. 2006; Reasor et al. 2000; Black et al. 2002) and simulated (Wang 2002a). In the present case, the azimuthal propagation of VRWs at WN-2 interacting with the quasi-stationary WN-1 component plays an important role in generating the drastic fluctuations in the horizontal winds of Bonnie. The most striking example of the positive interaction occurs at 46.5 h (Fig. 13a), when the WN-2

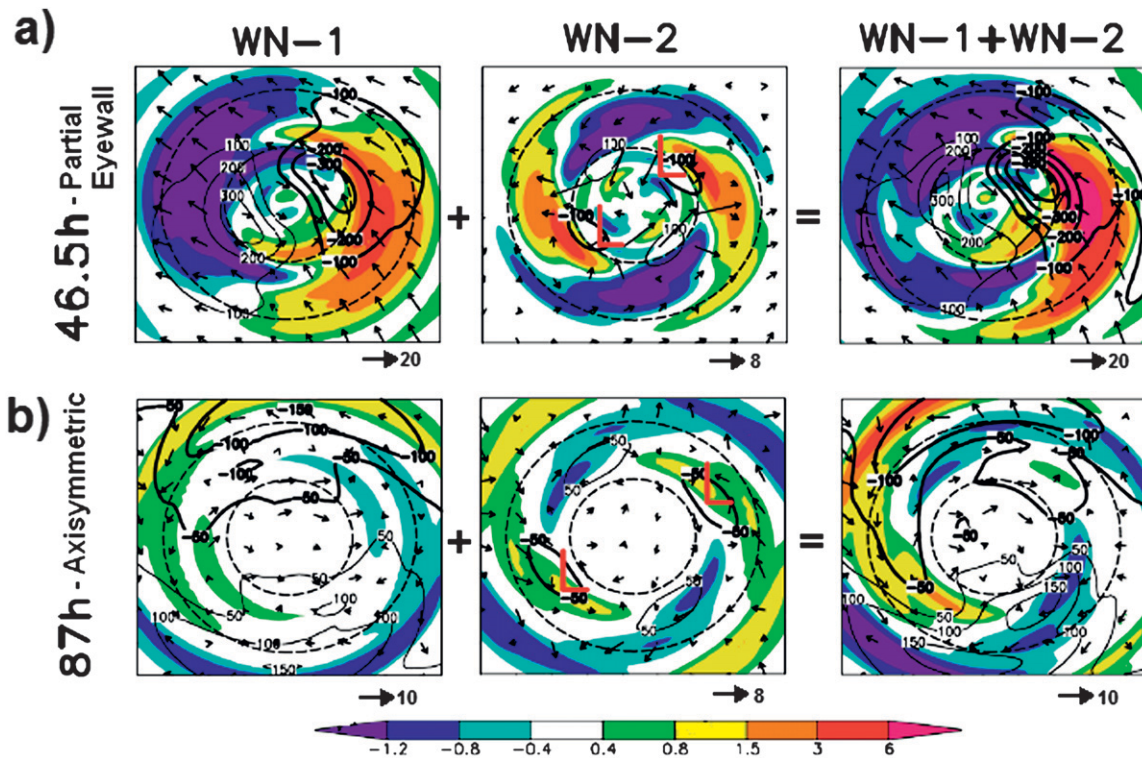


FIG. 12. Horizontal distribution of pressure perturbations at $z = 3$ km [contoured with thick (thin) lines for positive (negative) values], in-plane flow vectors at $z = 1.5$ km, and the averaged vertical motion in the 6–8-km layer (shaded) from the (a) 46.5- and (b) 87-h simulations. (left) WN-1 and (middle) WN-2 components are shown, together with (right) the sum of WN-1 and WN-2; and their corresponding pressure field is contoured at intervals of (a) 100 and (b) 50 Pa. Dashed circles represent radius rings at $R = 50$ km and $R = 100$ km. The symbol “L” denotes the location of a WN-2 low pressure feature.

pressure and vertical motion are in phase, and upward motion occurs downshear at the same location as the positive WN-1 vertical motion. In the subsequent 2 h, Bonnie undergoes a 5-hPa drop in the minimum central pressure (Fig. 1).

b. The axisymmetric eyewall stage

In contrast, during the 72–90-h period, the WN-0 component of vertical motion grows in magnitude, while the higher-order components decay (Fig. 10b). This indicates the completion of the eyewall replacement and the transition to axisymmetry (see Fig. 18a in Part I) by 87 h. As Fig. 14 shows, the eyewall replacement is also closely associated with the propagation of convective elements in the eyewall, but in a different fashion from that shown in Fig. 11. Specifically, as the vertical shear decays rapidly during this period (Fig. 8), convective elements are able to propagate around the full annulus of the storm. For example, at 84.5 h, there exists a single spiral rainband denoted B_1 , whose leading edge is located at $R = 50$ km in the northern half of the storm where the peak KE is located. As this rainband propagates cyclonically outward, it facilitates the production

of KE (i.e., KGEN) in the PBL. By 87 h, the convective element, now denoted B_2 , has made almost a half circle at $R = 50$ km. Meanwhile, the trailing convective band is active in producing KE, and now the KE maximum has filled more than 75% of the annulus at $R = 100$ km. By 88.5 h the leading edge of the spiral band B_3 has completed nearly a full circle around the annulus of the storm and the peak KE has propagated outward and remains near $R = 100$ km, effectively forming a new axisymmetric radius of maximum KE (RMK) at $R = 100$ km. In this way, the propagation of a single spiral rainband in a weak-sheared environment could facilitate the formation of a new eyewall. That is, a partial RMK at 85 h, $R = 60$ km, is replaced by an axisymmetric RMK with $R = 100$ km by 88.5 h. Subsequent intensification after 90 h (Fig. 1) is related to the contraction of this new eyewall prior to landfall (not shown).

It is evident from Fig. 12b that the abovementioned structures, after wave decomposition, are captured again using only the asymmetric structures (i.e., WN-1 and WN-2). The implication of this is that the eyewall replacement process can be described as an asymmetric process. The WN-1 component is smaller during this

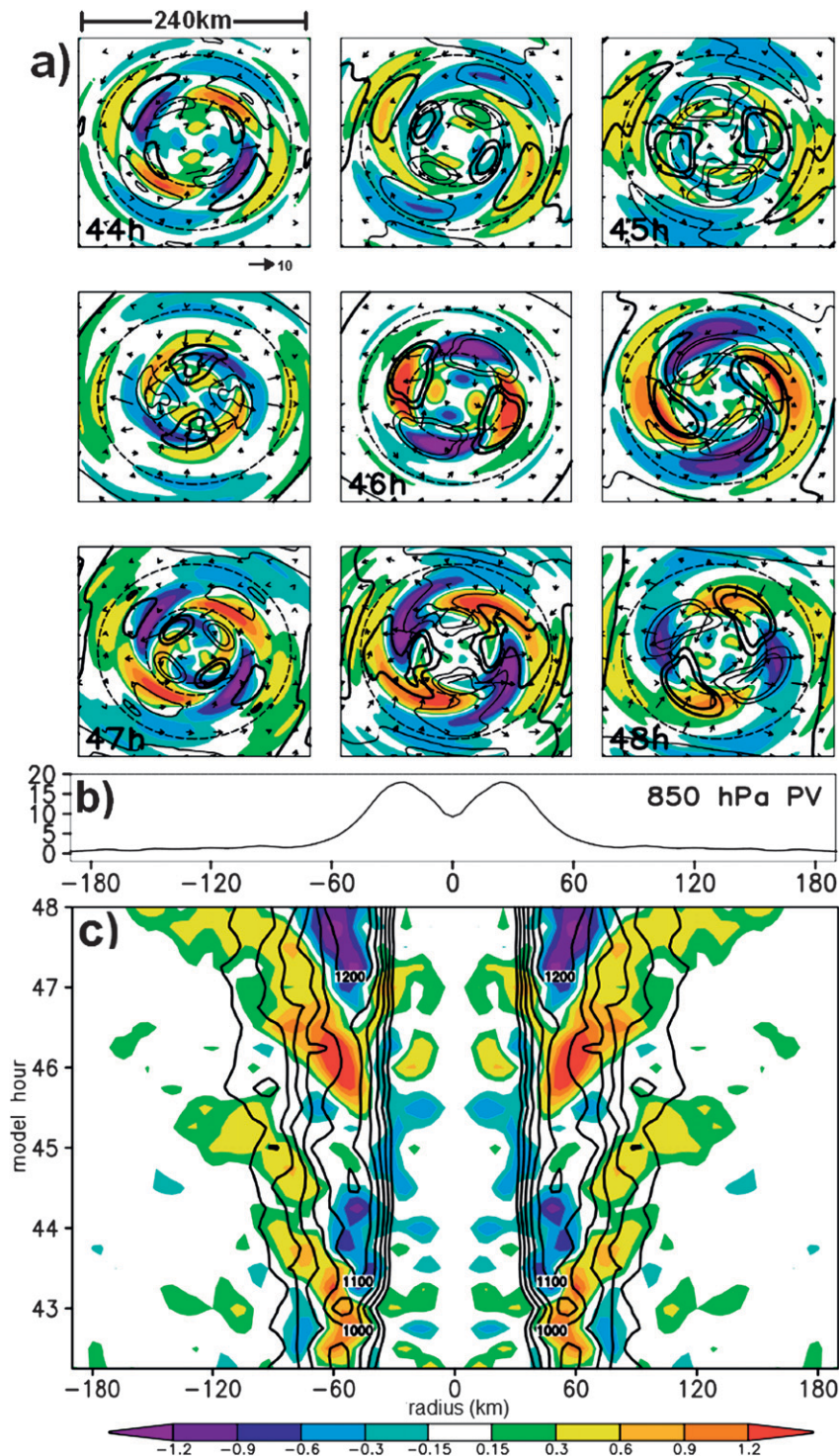


FIG. 13. (a) As in Fig. 11, but for the averaged WN-2 vertical motion in the 6–10-km layer (shaded), and WN-2 pressure perturbations [contoured at intervals of 25 Pa with thick (thin) lines for negative (positive) values] in the 2–3-km layer, superposed with the horizontal WN-2 flow vectors at $z = 1.5$ km. (b) West–east cross section, taken through the storm center, of the averaged 850-hPa PV during the 42–48-h period. (c) The radius–time plot of the averaged WN-2 vertical motion in the 6–10-km layer (shaded) and the averaged WN-0 KE in the 2–3-km layer (contoured at intervals of 100 J kg^{-1} for values greater than 600 J kg^{-1}). In (c), the time series is constructed by taking a west–east cross section through the storm center at 15-min intervals.

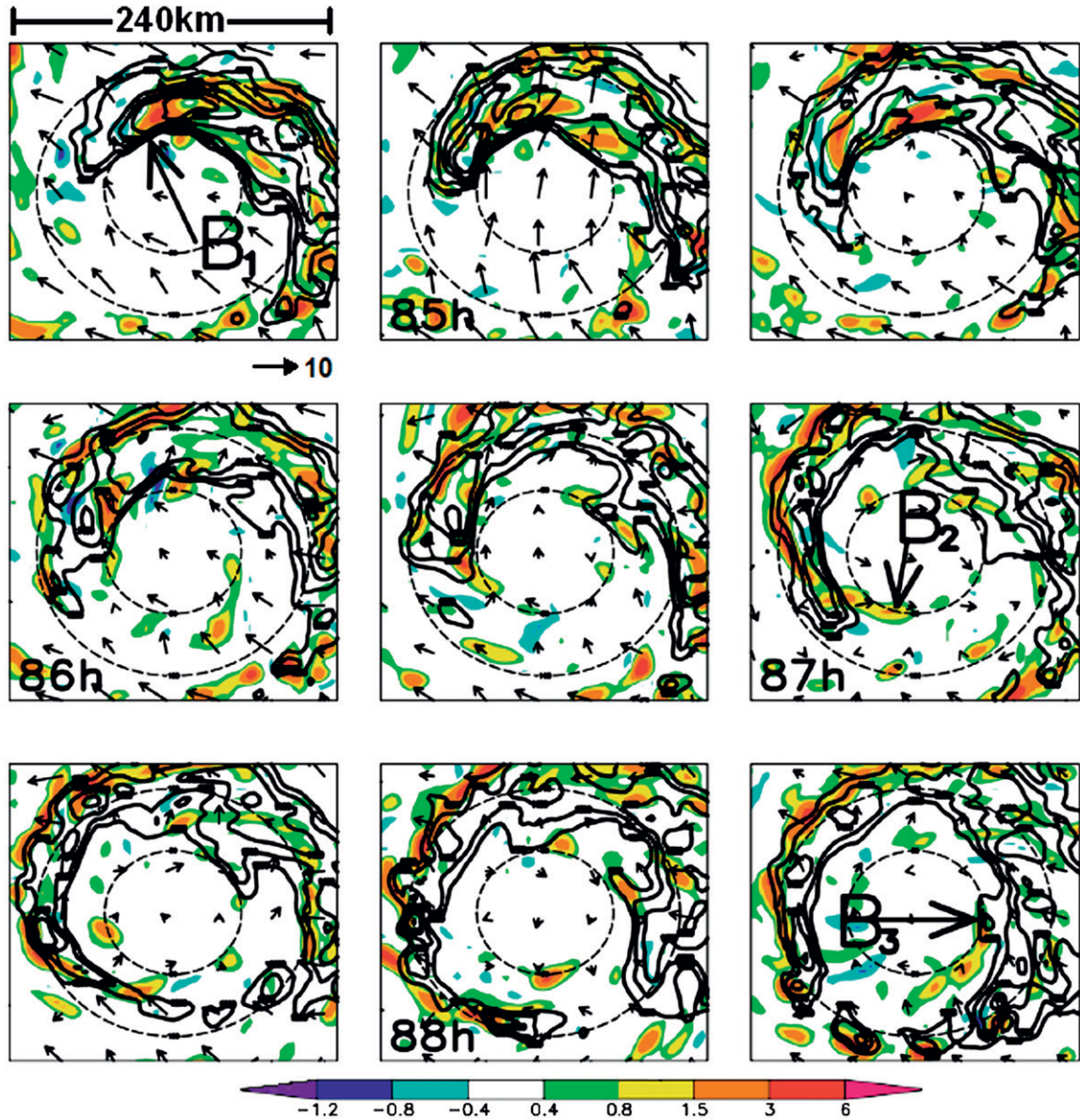


FIG. 14. As in Fig. 11, but from the 84.5–88.5-h simulations with KE contoured at intervals of 100 J kg^{-1} between 12 and $19 \times 10^2 \text{ J kg}^{-1}$; B_1 , B_2 , and B_3 denote the leading edge of a cyclonically propagating convective element.

later stage, as could be expected, as the vertical shear rapidly decreases (Fig. 8). Deep convection is well coupled with the WN-1 and WN-2 low pressure zones. Because the eyewall replacement appears to be facilitated by the propagating convective element, tracked by B_1 , B_2 , and B_3 in Fig. 14, we next analyze the evolution of WN-2 features associated with this convective element.

Figure 15a shows a full-circle propagation of a WN-2 pressure perturbation and its associated vertical motion during 84.5–88.5 h with the leading edge near $R = 60 \text{ km}$; it moves at approximately 30 m s^{-1} , which is roughly 67% of the mean tangential wind speed. The pressure

wave propagates slightly faster than the vertical motion wave, but they remain generally well coupled. In addition, the WN-2 waves propagate radially outward at a speed of 11 m s^{-1} down the PV gradient (cf. Figs. 15b,c). One can see from Fig. 15a that the vertical motion of WN-2 at $R = 50\text{--}120 \text{ km}$ increases in amplitude up to 87 h, indicating that major LHR/KGEN features are propagating radially outward. But the WN-2 amplitudes decrease during the period of 87–88.5 h, and a new RMK begins to emerge near $R = 120 \text{ km}$ (Fig. 15c). The implication of the coincident decrease in WN-2 energy and increase in WN-0 energy (see Fig. 10b) is that the

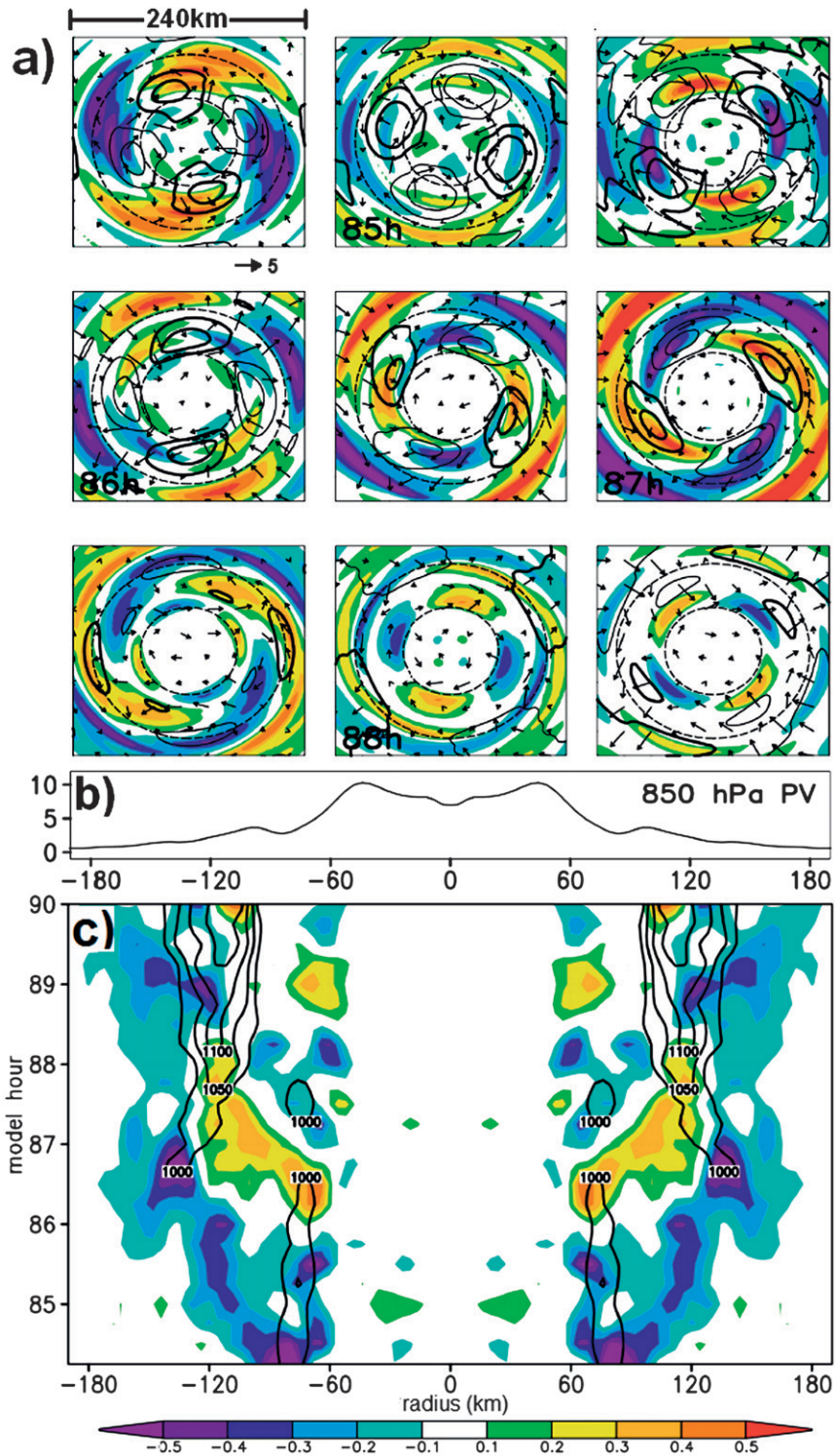


FIG. 15. As in Fig. 13, but from the (a) 84.5–88.5-h and (b) 84–90-h simulations, in which the WN-0 KE is contoured at intervals of 50 J kg^{-1} for values greater than 1000 J kg^{-1} during the eyewall replacement (i.e., the transition to axisymmetry).

outward-propagating WN-2 waves are being axisymmetrized, a process that can occur as they slow their radial propagation, undergo filamentation, and take on a more symmetric appearance (Montgomery and Kallenbach 1997).

7. Summary and conclusions

In this study, the energetic characteristics of TCs in relation to intensity and structural changes under different sheared conditions are analyzed using a cloud-resolving simulation of the life cycle of Hurricane Bonnie (1998) with the finest resolution of 4 km at 15-min intervals. In the presence of intense vertical shear, Bonnie exhibits a partial eyewall with an RMW of 50 km and large intensity fluctuations with quasi-regular periods of 2–5 h. Then, Bonnie undergoes an eyewall replacement as the vertical shear subsides below 12 m s^{-1} , and her intensity varies smoothly during the subsequent axisymmetric stage with an RMW of 100 km.

It is found that time series of BKE compare fairly well, though not exactly, to the sequence of intensity changes. A phase diagram is plotted, following Maclay et al. (2008), to show that Bonnie is bulk-energetically small during the partial eyewall stage but large after the eyewall replacement cycle. Most of the BKE is generated in the lowest 3 km of the eyewall, and its combination with the environmental KE flux divergence is balanced by the KE dissipation in the PBL. The LE supply from Bonnie's environment also plays an important role in determining the magnitude of LHR in the eyewall, but only less than 2% of the total LHR could be converted to KE. Results show that the conversion to KE could be negative on the upshear side of the eyewall due to the development of evaporatively driven moist downdrafts in the eyewall. It is also found that the storm-scale eddy KE is proportional to the magnitude of vertical shear, with most of the eddy KE concentrated in the PBL near the RMW.

Results show that the intensity fluctuations are closely related to the fluctuations in energy conversions through deep convection of varying intensity in the partial eyewall, rather than to "numerical noise." Because vertical shear acts to enhance (suppress) vertical motion downshear (upshear), convective cells undergo a cycle of growth on the downshear side and decay on the upshear side—a WN-1 phenomenon. That is, as the cells grow (decay), the enhanced (suppressed) KE production near the RMW in the PBL locally accelerates (decelerates) the maximum wind speed on the downshear (upshear) side.

Fourier decomposition of the flow fields shows convectively generated WN-2 perturbations that resemble VRWs propagating in the eyewall during both the asym-

metric and axisymmetric stages. That is, they adhere to VRW theory by propagating azimuthally at a speed slower than the mean tangential wind, and outward down the radial PV gradient. Moreover, convection associated with the WN-2 perturbations evolves in concert with the fluctuations in V_{MAX} during the partial eyewall stage. Similarly, a WN-2 perturbation, free from the constraint of vertical shear, exhibits cyclonic and outward propagation during the eyewall replacement cycle. Its radial propagation stalls at large radii, but the deep convection remains active and appears to facilitate the development of an outer eyewall. However, the timing and location of the eyewall replacement phenomenon appears to be determined by the large-scale flows, because VRWs do occur often in TCs.

Acknowledgments. We thank Dr. T. Zhu for providing the high-resolution data for the present study, and two anonymous reviewers for their helpful comments. This work was supported by ONR Grant N000140710186 and NASA Grant NNG05GR32G.

REFERENCES

- Black, M. L., and G. J. Holland, 1995: The boundary layer of Tropical Cyclone Kerry (1979). *Mon. Wea. Rev.*, **123**, 2007–2028.
- , J. F. Gamache, F. D. Marks Jr., C. E. Samsury, and H. E. Willoughby, 2002: Eastern Pacific Hurricanes Jimena of 1991 and Olivia of 1994: The effect of vertical wind shear on structure and intensity. *Mon. Wea. Rev.*, **130**, 2291–2312.
- Braun, S. A., 2002: A cloud-resolving simulation of Hurricane Bob (1991): Storm structure and eyewall buoyancy. *Mon. Wea. Rev.*, **130**, 1573–1592.
- Corbosiero, K. L., J. Molinari, A. R. Aiyyer, and M. L. Black, 2006: The structure and evolution of Hurricane Elena (1995). Part II: Convective asymmetries and evidence for vortex-Rossby waves. *Mon. Wea. Rev.*, **134**, 3073–3091.
- Dudhia, J., 1993: A nonhydrostatic version of the Penn State-NCAR Mesoscale Model: Validation tests and simulation of an Atlantic cyclone and cold front. *Mon. Wea. Rev.*, **121**, 1493–1513.
- Dutton, J. A., 1976: *The Ceaseless Wind*. McGraw-Hill, 576 pp.
- Frank, W. M., 1977: The structure and energetics of the tropical cyclone II. Dynamics and energetics. *Mon. Wea. Rev.*, **105**, 1136–1150.
- Hack, J. J., and W. H. Schubert, 1986: Nonlinear response of atmospheric vortices to heating by organized cumulus convection. *J. Atmos. Sci.*, **43**, 1559–1573.
- Heymsfield, G. M., J. B. Halverson, J. Simpson, L. Tian, and T. P. Bui, 2001: ER-2 Doppler radar investigations of the eyewall of Hurricane Bonnie during the Convection and Moisture Experiment-3. *J. Appl. Meteor.*, **40**, 1310–1330.
- Kieu, C. Q., and D.-L. Zhang, 2008: Genesis of Tropical Storm Eugene (2005) from merging vortices associated with ITCZ breakdowns. Part I: Observational and modeling analyses. *J. Atmos. Sci.*, **65**, 3419–3439.
- Kossin, J. P., W. H. Schubert, and M. T. Montgomery, 2000: Unstable interactions between a hurricane's primary eyewall and

- a secondary region of enhanced vorticity. *J. Atmos. Sci.*, **57**, 3893–3917.
- Liu, Y., D.-L. Zhang, and M. K. Yau, 1997: A multiscale numerical study of Hurricane Andrew (1992). Part I: Explicit simulation and verification. *Mon. Wea. Rev.*, **125**, 3073–3093.
- Maclay, K. S., M. DeMaria, and T. H. Vonder Haar, 2008: Tropical cyclone inner-core kinetic energy evolution. *Mon. Wea. Rev.*, **136**, 4882–4898.
- McBride, J. L., 1981: Observational analysis of tropical cyclone formation. Part III: Budget analysis. *J. Atmos. Sci.*, **38**, 1152–1166.
- Molinari, J., and D. Vollaro, 2008: Extreme helicity and intense convective towers in Hurricane Bonnie. *Mon. Wea. Rev.*, **136**, 4355–4372.
- Montgomery, M. T., and R. J. Kallenbach, 1997: A theory for vortex Rossby waves and its application to spiral bands and intensity changes in hurricanes. *Quart. J. Roy. Meteor. Soc.*, **123**, 435–465.
- Powell, M., and T. Reinhold, 2007: Tropical cyclone destructive potential by integrated kinetic energy. *Bull. Amer. Meteor. Soc.*, **88**, 1–14.
- Reasor, P. D., and M. T. Montgomery, 2001: Three-dimensional alignment and corotation of weak, TC-like vortices via linear vortex Rossby waves. *J. Atmos. Sci.*, **58**, 2306–2330.
- , —, F. D. Marks Jr., and J. F. Gamache, 2000: Low wave-number structure and evolution of the hurricane inner core observed by airborne dual-Doppler radar. *Mon. Wea. Rev.*, **128**, 1653–1680.
- Tuleya, R. E., and Y. Kurihara, 1975: The energy and angular momentum budgets of a three-dimensional tropical cyclone model. *J. Atmos. Sci.*, **32**, 287–301.
- Wang, Y., 2001: An explicit simulation of tropical cyclones with a triply nested movable mesh primitive equation model: TCM3. Part I: Model description and control experiment. *Mon. Wea. Rev.*, **129**, 1370–1394.
- , 2002a: Vortex Rossby waves in a numerically simulated tropical cyclone. Part I: Overall structure, potential vorticity, and kinetic energy budgets. *J. Atmos. Sci.*, **59**, 1213–1238.
- , 2002b: Vortex Rossby waves in a numerically simulated tropical cyclone. Part II: The role in tropical cyclone structure and intensity changes. *J. Atmos. Sci.*, **59**, 1239–1262.
- Zhang, D.-L., and C. Q. Kieu, 2006: Potential vorticity diagnosis of a simulated hurricane. Part II: Quasi-balanced contributions to forced secondary circulations. *J. Atmos. Sci.*, **63**, 2898–2914.
- , Y. Liu, and M. K. Yau, 2001: A multiscale numerical study of Hurricane Andrew (1992). Part IV: Unbalanced flows. *Mon. Wea. Rev.*, **129**, 92–107.
- , —, and —, 2002: A multiscale numerical study of Hurricane Andrew (1992). Part V: Inner-core thermodynamics. *Mon. Wea. Rev.*, **130**, 2745–2763.
- Zhu, T., and D.-L. Zhang, 2006a: Numerical simulation of Hurricane Bonnie (1998). Part II: Sensitivity to varying cloud microphysical processes. *J. Atmos. Sci.*, **63**, 109–126.
- , and —, 2006b: The impact of the storm-induced SST cooling on hurricane intensity. *Adv. Atmos. Sci.*, **23**, 14–22.
- , —, and F. Weng, 2004: Numerical simulation of Hurricane Bonnie (1998). Part I: Eyewall evolution and intensity changes. *Mon. Wea. Rev.*, **132**, 225–241.